Winding Layout Considerations for Variable-Pole Induction Motors in Electric Vehicles

Elie Libbos, *Graduate Student Member, IEEE*, Elisa Krause, *Graduate Student Member, IEEE*, Arijit Banerjee, *Senior Member, IEEE*, and Philip T. Krein, *Life Fellow, IEEE*

***Abstract*— Winding layout plays a crucial role in enabling variable-pole operation in an induction machine (IM). Several winding design alternatives, which consist of toroidal and distributed single- and double-layer windings, have been shown to increase speed range and improve partial load efficiency in traction applications. These windings have different pole-changing capability, end-winding length, leakage, harmonic content, and inverter requirements. This article compares these winding alternatives with a generalized variable-pole machine design framework that captures the impact of winding selection on key performance metrics such as losses, volume, and torque–speed envelop. This framework shows that the core aspect ratio, defined as ratio of stack length to rotor diameter, selected to minimize losses depends on whether a distributed or toroidal winding is used. When a toroidally wound IM is designed with a low aspect ratio, it can provide the largest torque–speed envelop with highest efficiency over a wide speed range. An experimental toroidally wound IM driven by an 18-leg converter is used to validate the design framework. The experimental setup is configured externally to emulate a single-layer winding and to show benefits gained from the extra pole-changing flexibility of a toroidal winding.**

***Index Terms*— Electric vehicles (EVs), induction machine (IM), motor design, motor windings, multiphase drives, pole changing, traction.**

I. Introduction

ELECTRIC vehicle (EV) drivetrains require power-dense and efficient motors, operating over a wide speed range [1], [2], [3]. Conventionally, the torque–speed envelop of fixed-pole induction machines (IMs) is constrained by the inverter output voltage at the base speed. This reduces the torque capability at the maximum speed, as shown in Fig. 1 [4], [5], [6]. Overdesigning the inverter to improve the envelop decreased the efficiency and power density in [7] and [8]. Alternatively, torque capability above the base speed can be improved substantially by electronically reconfiguring the IM to lower pole counts, as shown in Fig. 1 [9], [10], [11], [12]. Specifically, Libbos et al. [8] showed that a multileg inverter can improve the high-speed torque capability by a factor of 2.2×, while simultaneously achieving higher efficiency, with less dc link capacitance, and simpler thermal management, compared with a conventional three-leg fixed-pole design with the same motor.

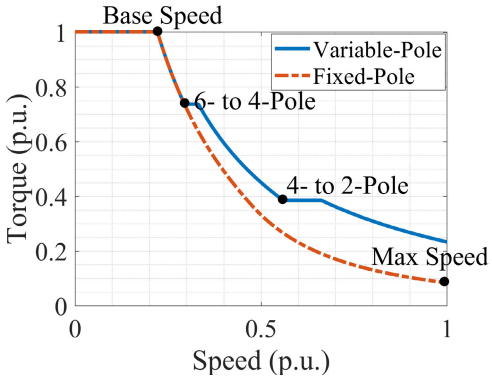

Fig. 1. Torque–speed characteristic of an IM when operated with a fixed six-pole configuration versus variable six-, four-, and two-pole operations. High-speed torque capability is improved by reconfiguring to lower pole counts.

Electronic pole reconfiguration requires a stator winding layout with increased winding accessibility. Several stator winding design approaches have been investigated in the literature for variable-pole IMs [9], [10], [11], [13], [14], [15], [16], [17], [18], [19], [20], [21] and typical examples are shown in Fig. 2. Libbos et al. [7], Miller et al. [10], Libbos et al. [11], Magill [12], and Libbos et al. [13] used toroidal windings (Gramme windings) to help achieve a wide set of pole counts through independent current control of each coil based on the number of inverter legs. For example, a 36-slot machine driven by an 18-leg converter can be reconfigured to six-, four-, and two-pole count [11]. Another option is to use a conventional single-layer distributed winding, which reduces the number of inverter legs by half at the cost of losing flexibility to reconfigure to four poles [14], [17], [18], [19]. However, the single-layer winding is designed for the lowest pole count (two poles in this case) which leads to a long end-winding. Selecting a short-pitched, double-layer winding reduces the end-winding length [20], [22], but this option reduces the winding factor at the higher pole count, sacrificing the torque capability in the low-speed region. Another conventional pole-changing option is to use a Dahlander winding which allows for a single 2:1 pole combination, e.g., eight-/four-pole or four-/two-pole [23], [24], [25]. An electronically reconfigurable alternative to the Dahlander winding was explored based on a four-pole double-layer 120° phase belt design driven by a six-phase inverter [9], [15], [16].

Manuscript received 3 July 2022; revised 22 September 2022 and 22 November 2022; accepted 19 February 2023. Date of publication 23 February 2023; date of current version 21 December 2023. This work was supported in part by the Grainger Center for Electric Machinery and Electromechanics and in part by the Power Optimization of Electro-Thermal Systems (POETS) NSF Engineering Research Center at the University of Illinois under Award R2.037.22. *(Corresponding author: Elie Libbos.)*

Elie Libbos, Arijit Banerjee, and Philip T. Krein are with the Department of Electrical and Computer Engineering, University of Illinois at Urbana-Champaign, Urbana, IL 61820 USA (e-mail: elibbos2@illinois.edu).

Elisa Krause is with the Department of Electrical Engineering and Computer Sciences, University of California, Berkeley, CA 94720 USA.

Digital Object Identifier 10.1109/TTE.2023.3248444

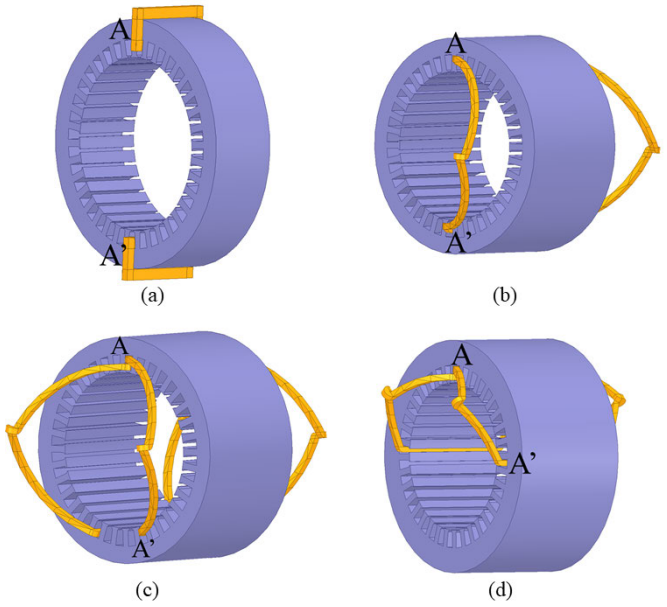

Fig. 2. Possible winding configurations for achieving variable-pole operation. (a) Toroidal winding that can reconfigure to the six-, four-, and two-pole operations [10], [11], [12], [13]. (b) Distributed single-layer winding designed for $p_{\min} = 2$ that can reconfigure to the six- and two-pole operations [14], [17], [18], [19]. (c) Double-layer winding with 20° pitch angle [20], [22]. (d) Double-layer version with 120° phase belt designed at $p_{\max} = 4$ that can reconfigure to the two-pole operation [9], [15], [16].

The IM can be reconfigured to two-pole by reversing the current of one coil group. While this approach leads to smaller end-winding compared with conventional distributed windings, it suffers from a low winding factor when operated at two-pole [16]. In summary, double-layer winding layout options are limited by a lower winding factor at either the higher or lower pole count when used in variable-pole operation. The existing body of literature has proposed several winding options for electronic pole reconfiguration, the selection of which impacts both the torque–speed envelop and end-winding losses and leakage. Thus, an open question remains: How do these winding options compare in terms of torque production, efficiency, power density, and torque–speed envelop in a variable-pole design space?

The main contribution of this article is a variable-pole IM winding study that compares various winding layouts in terms of key performance metrics by tailoring core design to the winding type. Analysis shows that the aspect ratio, defined as the ratio of the stack length to the rotor diameter, plays an important role in reducing the end-turn length and, therefore, in reducing copper loss and leakage inductance. Distributed windings favor a smaller rotor diameter, which can be achieved at the expense of longer stack length, while toroidal winding length reduces with shorter stack length. A toroidal winding layout with a low aspect ratio is shown to provide the highest flexibility in terms of pole-changing capability, maximizing the achievable torque–speed envelop along with higher power density and efficiency. Its extra flexibility to reconfigure to four poles improves the efficiency in the intermediate torque–speed range by reducing core and copper losses. An experimental toroidally wound IM is used to validate the analysis and the results. The setup is configured externally to emulate a single-layer winding for comparison. Hardware results validate the improvement in the torque–speed envelop and efficiency improvement from the extra pole-changing flexibility of a toroidal design. The high number of inverter legs leads to fault-tolerant operation even when two of the inverter legs fail.

TABLE I
ELECTRONIC POLE-CHANGING FOR ALL FOUR WINDINGS USING PPM. $\Delta\theta_p$ IS THE MODULATED PHASE SHIFT BETWEEN TWO SUCCESSIVE WINDINGS IN FIG. 3 (E.G., C1 AND C2)

Winding	$\Delta\theta_2$	$\Delta\theta_4$	$\Delta\theta_6$
Toroidal (a)	20°	40°	60°
Distributed (b) and (c)	40°	N/A	120°
Distributed (d)	60°	120°	N/A

The rest of the article is organized as follows. Section II shows comparison of the four winding options from an achievable pole selection perspective and their impact on the harmonic content of the airgap flux density. Section III presents the design framework that captures the impact of the aspect ratio on efficiency and power density while accounting for the different winding layouts. Finite element analysis (FEA) is used to verify and refine the analytically obtained design variables such as the stack length, airgap diameter, and yoke depth. Section IV shows comparison of the torque–speed envelop and efficiency over the entire operating regime. Section V uses an experimental toroidally wound 36-slot IM driven by an 18-leg converter to validate the analysis. Section VI concludes the article.

II. WINDING OPTIONS FOR VARIABLE-POLE IM

This section shows comparison of the four winding layouts in terms of their winding factors, stator magnetomotive force (MMF) total harmonic distortion (THD), differential leakage, and achievable pole counts. As an example, a 36-slot stator is considered and the maximum number of inverter legs is limited to 18. Fig. 3 shows the winding distributions for the four layouts. The toroidal winding (option a) allows the most flexible excitation pattern as the physical coil pitch does not act as an additional constraint [10], [11], [12]. To connect the 36-slot stator to an 18-leg inverter, coils in adjacent slots are connected in series to form an 18-terminal stator winding [11]. This configuration enables reconfiguring the IM to a wide range of pole counts, including six, four, and two. Pole changing is achieved by applying phase shifts between two adjacent independent windings (e.g., C1 and C2 in Fig. 3), using a technique known as pole-phase modulation (PPM) [10]. To achieve pole count p, phase shift $\Delta\theta_p$ given by

$$\Delta\theta_p = \frac{2\pi}{n_{\text{inv}}}\frac{p}{2} \tag{1}$$

is introduced, where n_{inv} is the number of inverter legs. Table I summarizes the required phase shifts to enable the two-, four-, and six-pole operations. In the distributed single-layer winding layout (option b), the number of inverter legs reduces to nine as each coil spans two slots (e.g., C1 in slot 1 has a return conductor C1' in slot 19), as shown in Fig. 2. This winding is designed as a standard two-pole distributed winding and can be

Toroidal																																		
	Slot number	1	2	3	4	5	6	7	8	9	10	11	12	13	14	15	16	17	18	19	20	21	22	23	24	25	26	27	28	29	30	31	32	33	34	35	36
	Coil	C1	C1	C2	C2	C3	C3	C4	C4	C5	C5	C6	C6	C7	C7	C8	C8	C9	C9	C10	C10	C11	C11	C12	C12	C13	C13	C14	C14	C15	C15	C16	C16	C17	C17	C18	C18
	Inverter Leg	1	N	2	N	3	N	4	N	5	N	6	N	7	N	8	N	9	N	10	N	11	N	12	N	13	N	14	N	15	N	16	N	17	N	18	N

Single Layer Distributed																																				
	Slot number	1	2	3	4	5	6	7	8	9	10	11	12	13	14	15	16	17	18	19	20	21	22	23	24	25	26	27	28	29	30	31	32	33	34	35	36
	Coil	C1	C1	C6'	C6'	C2	C2	C7'	C7'	C3	C3	C8'	C8'	C4	C4	C9'	C9'	C5	C5	C1'	C1'	C6	C6	C2'	C2'	C7	C7	C3'	C3'	C8	C8	C4'	C4'	C9	C9	C5'	C5'
	Inverter Leg	1			N	2			N	3			N	4			N	5			N	6			N	7			N	8			N	9			N

Double Layer distributed with 20° short-pitch																																				
	Slot number	1	2	3	4	5	6	7	8	9	10	11	12	13	14	15	16	17	18	19	20	21	22	23	24	25	26	27	28	29	30	31	32	33	34	35	36
	Top layer	C1	C1	C6'	C6'	C2	C2	C7'	C7'	C3	C3	C8'	C8'	C4	C4	C9'	C9'	C5	C5	C1'	C1'	C6	C6	C2'	C2'	C7	C7	C3'	C3'	C8	C8	C4'	C4'	C9	C9	C5'	C5'
	Bottom layer	C6'	C6'	C2	C2	C7'	C7'	C3	C3	C8'	C8'	C4	C4	C9'	C9'	C5	C5	C1'	C1'	C6	C6	C2'	C2'	C7	C7	C3'	C3'	C8	C8	C4'	C4'	C9	C9	C5'	C5'	C1	C1
	Inverter Leg (top layer)	1			N	2			N	3			N	4			N	5			N	6			N	7			N	8			N	9			N

Double Layer with 120° phase belt																																				
	Slot number	1	2	3	4	5	6	7	8	9	10	11	12	13	14	15	16	17	18	19	20	21	22	23	24	25	26	27	28	29	30	31	32	33	34	35	36
	Top Layer	C1	C1	C1	C1	C1	C1	C2	C2	C2	C2	C2	C2	C3	C3	C3	C3	C3	C3	C4	C4	C4	C4	C4	C4	C5	C5	C5	C5	C5	C5	C6	C6	C6	C6	C6	C6
	Bottom Layer	C5'	C5'	C5'	C6'	C6'	C6'	C6'	C6'	C6'	C1'	C1'	C1'	C1'	C1'	C1'	C2'	C2'	C2'	C2'	C2'	C2'	C2'	C3'	C3'	C3'	C3'	C3'	C4'	C4'	C4'	C4'	C4'	C4'	C5'	C5'	C5'
	Inverter Leg (top layer)	1						2						3						4						5						6					
	Inverter leg (bottom layer)			N						N						N						N						N						N			

Fig. 3. Winding layout and inverter connections for variable-pole IM for the four alternatives for a 36-slot machine. For the toroidal winding, the return conductors are on the outer periphery of the stator core and, hence, not shown.

TABLE II

COMPARISON OF FUNDAMENTAL WINDING FACTOR AND THD OF STATOR MMF FOR ALL FOUR WINDING TYPES OF FIGS. 2 AND 3 WITH $Q_s = 36$. THE THD AND DIFFERENTIAL LEAKAGE COEFFICIENT ARE COMPUTED ANALYTICALLY USING THE MODEL IN SECTION II

Winding layout	Inverter legs	Feasible pole counts	Fundamental winding factor	THD(%)	Differential leakage σ_d
Torroidal winding (a)	18	6-pole	0.966	16.8	0.0284
		4-pole	0.985	10.6	0.0112
		2-pole	0.992	5	0.0026
Single layer distributed (b)	9	6-pole	0.966	16.8	0.0284
		2-pole	0.992	5	0.0026
Double layer distributed with 20° short pitch (c)	9	6-pole	0.834	16.8	0.0284
		2-pole	0.981	5	0.0026
Double layer distributed with 120° phase belt (d)	6	4-pole	0.8312	11.85	0.014
		2-pole	0.676	7.2	0.0028

reconfigured to six-pole by varying $\Delta\theta_p$, as shown in Table I. This layout cannot generate a four-pole pattern because the physical coil pitch constrains diametrically opposite slots (e.g., C1 in slot 1 and C1' in slot 19) to be out-of-phase while a four-pole configuration requires them to be in-phase. Option c considers a double-layer, two-pole winding short-pitched by 20° with the same inverter configuration as (b). Finally, a four-pole double-layer winding with a 120° phase belt that can be reconfigured for the two-pole operation [9], [16] is considered as option d. Because of the lower $p_{\max}$ to $p_{\min}$ ratio, this configuration requires only six inverter legs, the lowest among all the four windings.

The next step is to compute the fundamental winding factors and stator MMF THD of the four winding options using winding functions. The winding function of an m-phase/p-pole excitation is given by [26]

$$N(\theta) = \frac{2N_c}{\pi}\sum_{v=1}^{\infty} k_w(p, v)\frac{\sin(v\theta)}{v} \tag{2}$$

where N_c is the number of conductors in a slot, v is the harmonic number, q is the number of slots per pole per phase, θ is the electrical angle, and $k_w(p, v)$ is the winding factor. $k_w(p, v)$ and phase number m are given by

$$k_w(p, v) = \cos\left(\frac{\mathrm{vp}\alpha}{2\mathrm{p_{min}}}\right)\frac{\sin\left(\mathrm{v}\frac{\pi \mathrm{qp}}{2\mathrm{Q_s}}\right)}{\mathrm{qsin}\left(\mathrm{v}\frac{\pi \mathrm{p}}{2\mathrm{Q_s}}\right)} \tag{3}$$

$$m = \frac{Q_s}{qp} \tag{4}$$

where α is the short pitch angle at the minimum pole count $p_{\min}$, and Q_s is the total number of slots. Using (3) and assuming $Q_s = 36$, the fundamental winding factor and the THD of each winding configuration for all the feasible pole counts are computed and summarized in Table II. THD and differential leakage coefficient σ_d are computed using [26]

$$\mathrm{THD} = \frac{\sqrt{\sum_{v=2}^{\infty}\left(\frac{k_w(p,v)}{v}\right)^2}}{k_w(p, 1)} \tag{5}$$

$$\sigma_d = \frac{\sum_{v=2}^{\infty}\left(\frac{k_w(p,v)}{v}\right)^2}{k_w^2(p, 1)}. \tag{6}$$

Toroidal and single-layer windings, driven by 18-leg and nine-leg inverters, respectively, have a relatively high winding factor for every pole configuration because they use high phase numbers. Double-layer windings have a low fundamental winding factor at either the higher or lower pole count, as short-pitching the winding at a given pole configuration leads to excessive flux cancellation in the other [9], [15], [16]. For example, shortening winding (c) by an angle $\alpha = 20°$ results in a 14.4% drop in winding factor for the six-pole operation and $\alpha = 40°$ leads to a 50% drop. All the winding types have highest THD and differential leakage at $p_{\max}$ which is used to deliver high torque at low speeds. Double-layer (d) has the lowest distortion and differential leakage near peak torque as it uses a four-pole configuration rather than a six-pole configuration which may help reduce stray losses. In general, the number of stator slots can be further increased to decrease THD in all the winding types. Section III uses

TABLE III
MOTOR DESIGN SPECIFICATIONS

Quantity	Value
Rated torque at base speed (N·m)	302
Base speed (RPM)	5000
Maximum speed (RPM)	22000
dc link voltage (V)	800
Current density J (A/mm^2)	10
Maximum fill factor	0.7
Core flux density B_{cs}	1.5 T
Teeth flux density B_{ts}	1.8 T
Number of stator slots Q_s	36
Airgap length g (mm)	0.5
Stator winding material	Copper
Rotor cage material	Copper
Core lamination	M19-24G

these winding factors to analytically design the stator for a given specification.

III. VARIABLE-POLE IM DESIGN CONSIDERING DIFFERENT WINDING LAYOUTS' FRAMEWORK

The design objective to be explored here is to deliver a specified torque at the base speed and maximize the torque capability at the maximum speed, by reconfiguring motor operation to lower pole counts using suitable stator excitation from a multileg drive. The design specifications and constraints are summarized in Table III. A copper rotor cage is used to reduce rotor bar losses [27], [28]. The machine aspect ratio is captured explicitly in the framework because it plays an important role in minimizing the winding length and volume. After selecting the variable-pole winding option based on Section II, the stator core is designed using the following approach.

1) Size the stator core to deliver rated torque at base speed.
2) Model electrical losses to capture the impact of winding design and aspect ratio on efficiency.
3) Refine stator and rotor slot designs using FEA.

A. Variable-Pole Core Design to Meet Torque Requirement at Base Speed

Variable-pole IMs are sized to deliver the rated torque T_{rated} at base speed using the largest pole count $p_{\max}$ [26]

$$T_{\text{rated}} = \frac{\pi}{4(1+\sigma_r)} D^2 l_e \, B_{g,p_{\max}} K_s k_{w,p_{\max}} \eta \cos\phi_{\text{gap}} \tag{7}$$

where D is the rotor diameter, $B_{g,p_{\max}}$ is the peak fundamental airgap flux density at $p_{\max}$, K_s is the surface current loading, σ_r is the rotor leakage coefficient, $k_{w,p_{\max}}$ is the fundamental winding factor at $p_{\max}$, η is the estimated motor efficiency, and $\cos\phi_{\text{gap}}$ is the estimated machine power factor. Sizing the machine to deliver rated torque using the highest pole count helps minimize the stator yoke thickness given by

$$d_{\text{cs}} = \frac{B_{g,p_{\max}} D}{B_{\text{cs}} p_{\max}} \tag{8}$$

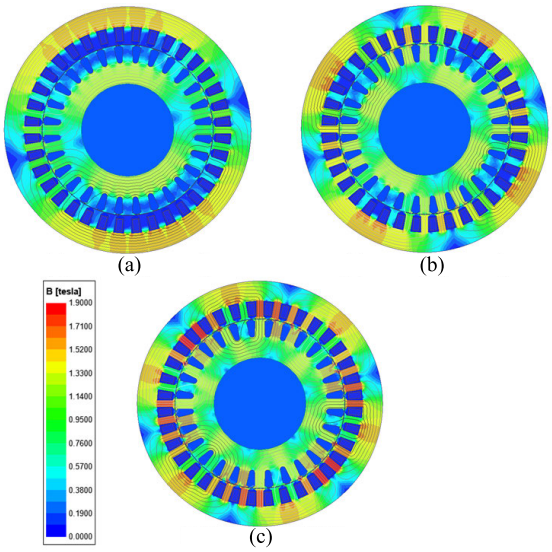

Fig. 4. FEA simulation of flux lines and density for the six-, four-, and two-pole operations using steady-state current excitation under no-load condition with rated magnetizing current. The peak fundamental airgap flux density B_g is marked. The results are summarized in Table IV. (a) Two-pole ($B_g = 0.36$ T). (b) Four-pole ($B_g = 0.66$ T). (c) Six-pole ($B_g = 0.89$ T).

TABLE IV
PEAK AIRGAP FLUX DENSITY AS A FUNCTION OF POLE COUNT FOR ALL WINDINGS. WINDING (1) FEA SIMULATIONS ARE ILLUSTRATED IN FIG. 4

Design	p	$B_{g,p}$ (T)	B_{cs} (T)	B_{ts} (T)
(1)	6-pole	0.89	1.5	1.9
(1)	4-pole	0.66	1.5	1.4
(1)	2-pole	0.36	1.5	0.82
(2)	6-pole	0.9	1.5	1.89
(2)	2-pole	0.37	1.5	0.80
(3)	6-pole	0.88	1.5	1.87
(3)	2-pole	0.35	1.5	0.82
(4)	4-pole	0.87	1.49	1.89
(4)	2-pole	0.44	1.5	0.97

where B_{cs} is the yoke flux density. Selection of this thickness limits the achievable peak airgap flux density at other operating pole counts p given by

$$B_{g,p} = \frac{p}{p_{\max}} B_{g,p_{\max}}. \tag{9}$$

Fig. 4 and Table IV illustrate the impact of pole changing on the airgap and core flux densities for a toroidal winding layout. For the same core flux density limit, lower pole counts (four- and two-pole) can push a smaller airgap flux density than six-pole. Because lower pole counts are only used with a partial flux density, variable-pole IMs benefit from both a smaller back yoke of higher pole count designs and improved high-speed torque of lower pole configurations. Although in this analysis the airgap flux density is assumed to be sinusoidal, the actual airgap flux density has harmonics due to winding distribution, stator slotting effects, and saturation, as explained in Section II and shown in Fig. 5. As the average of the actual airgap flux density is higher compared with

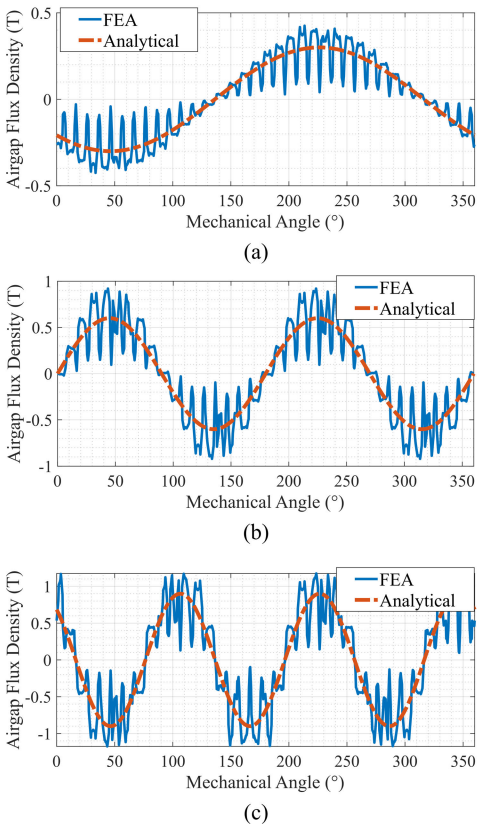

Fig. 5. FEA and analytical airgap flux densities for (a) two-, (b) four-, and (c) six-pole operations under the same conditions as Fig. 4.

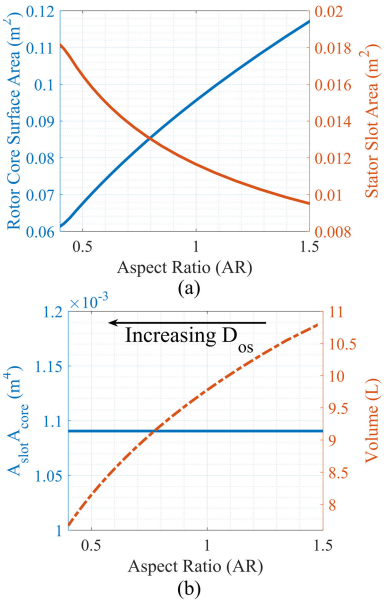

Fig. 6. Aspect ratio impact (a) slot and core areas A_{slot} and A_{core} and (b) machine volume. All the machines sized to deliver T_{rated} at ω_b using the same J_s and B_g and core flux densities, with the winding factor set to $k_w = 0.96$ for all the designs.

the sinusoidal assumption, the FEA solutions in Fig. 4 show localized tooth flux densities beyond 1.8 T. This mismatch can be accounted for analytically by introducing a scaling factor α_p in (8) and (9) [29] and using a sufficient number of sampling points in FEA to accurately represent harmonics.

By approximating stator slots as trapezoids as in [9], (7) can be rewritten as

$$T_{\text{rated}} = \frac{1}{2\sqrt{2}\pi(1+\sigma_r)} A_{\text{slot}} A_{\text{core}} J_s B_{g,p_{\max}} k_w \eta \cos\phi_{\text{gap}} \quad (10)$$

where A_{slot} is the total slot area occupied by stator windings, A_{core} is the rotor core surface area, and J_s is the stator current density. For given flux and current densities, (10) shows that the product $A_{\text{core}}A_{\text{slot}}$ must be constant. Using (7)–(10), the core dimensions are selected to meet the rated torque specification in Table III and illustrate the impact of A_{core} and A_{slot} on the active machine volume. Fig. 6(a) shows that there is a tradeoff between A_{core} and A_{slot}. Cores with smaller A_{slot} require larger A_{core} to maintain the same peak torque capability. This is because for a given J_s, reducing A_{slot} decreases the net current which is traded off against a larger magnetic flux achieved by increasing A_{core}. The choice between a larger A_{slot} or A_{core} is a tradeoff between net current and magnetic flux. Fig. 6(b) shows that core designs with larger A_{slot} and smaller A_{core} have smaller volume. Thus, lower aspect ratio designs, illustrated in Fig. 2(a), require smaller active volume to produce the same torque, as shown in Fig. 6, because their larger diameter D accommodates a larger net current. Eventually, tip speed and mechanical requirements provide a lower bound constraint on aspect ratio.

B. Impact of Aspect Ratio on Electrical Efficiency

The next step is to quantify the impact of winding layout on stator copper loss, which is influenced by the total winding length including the overhang. The toroidal winding length is

$$l_{\text{wind,tor}} = 2(d_{\text{cs}} + l_e) + l_{\text{OH}} \quad (11)$$

where l_{OH} is the overhang length, assumed to be 10% of the winding length. The winding lengths for winding options (b)–(d) are given by

$$l_{\text{wind,SL}} = \left(\frac{\pi D}{p_{\min}} + l_e\right) + l_{\text{OH}} \quad (12)$$

$$l_{\text{wind,DL1}} = \left(\frac{\pi D}{p_{\min}} + l_e\right)\left(1 - \frac{\alpha}{\pi}\right) + l_{\text{OH}} \quad (13)$$

$$l_{\text{wind,DL2}} = \left(\frac{\pi D}{p_{\max}} + l_e\right) + l_{\text{OH}}. \quad (14)$$

Minimizing the end-winding length and its associated losses looks different for toroidal and distributed windings. Distributed windings favor a shorter rotor diameter, which can be achieved at the expense of larger stack length, while toroidal winding length reduces with shorter stack length. For example, Wan et al. [30] used toroidal windings for a high-speed permanent-magnet alternator design with large diameter to reduce the end-winding length and its extra losses compared with a two-pole distributed winding. However, in the case of a large stack length-to-diameter ratio, toroidal windings had more copper losses compared with a distributed double-layer design [22].

TABLE V
DESIGN SUMMARY OF FOUR WINDING OPTIONS TO MEET SPECIFICATIONS

	(1)	(2)	(3)	(4)
Winding type	Toroidal	Single-layer	Double-layer	Double-layer
Possible pole configuration	6-, 4- and 2-pole	6- and 2-pole	6- and 2-pole	4- and 2-pole
Rated torque at base speed (N·m)	302	302	302	302
Torque at maximum speed (N·m)	71	57.4	63.4	48.4
Stator current density (A/mm^2)	10	10	10	10
Outer diameter D_{os} (mm)	320	270	282	295
Inner diameter D_{is} (mm)	220	185.4	194	186.4
Stack length l_e (mm)	89.5	148.4	155	149.1
Active volume V (L)	7.2	8.5	9.7	10.2
Aspect ratio	0.4	0.8	0.8	0.8
Rotor surface area (cm^2)	624	860.2	946	873
Total stator slot area (cm^2)	95	76	79	79
Active weight (kg)	57.5	67	76.7	79
Stator winding weight (kg)	10.2	16	19.3	13.1
Coil turn length (mm)	252	510	504	343
Stator leakage parameter (σ_s)	0.055	0.117	0.103	0.057
Stator copper losses (kW)	2.4	5.4	3.6	3.0
Rotor copper losses (kW)	1.1	1.6	1.1	1.3
Core losses (kW)	1.1	1.3	1.7	1.2
Rated Electrical Efficiency (%)	97.1	95.1	96	96.5

The stator and rotor copper losses $P_{\text{cu},s}$ and $P_{\text{cu},r}$ can be estimated as

$$P_{\text{cu},s} = F_s(\alpha)\rho_{\text{cu}} Q_s l_{\text{wind},s} A_{\text{slot}} k_{\text{cu}} J_s^2 \tag{15}$$

$$P_{\text{cu},r} = \rho_{\text{cu}} V_{\text{cage}} J_r^2 \tag{16}$$

where k_{cu} is the coil fill factor, $F_s(\alpha)$ is the ratio of ac-to-dc resistance [26], V_{cage} is the cage volume, and ρ_{cu} is the copper resistivity. The core losses are modeled using a Steinmetz equation

$$P_{\text{core}} = C_h f_e B_{\text{core}}^{\gamma} + C_e f_e^2 B_{\text{core}}^2 \tag{17}$$

where C_h and C_e are the hysteresis and eddy current coefficients, respectively, and B_{core} is the peak stator flux density.

Fig. 7 shows the impact of the aspect ratio on electrical efficiency, which consists of copper and core losses at 50 °C, at base and maximum speed. The highest pole $p_{\max}$ is used at ω_b and $p_{\min}$ is used at $\omega_{\max}$. The efficiency of the toroidally wound IM increases with decreasing aspect ratio because this minimizes the stator winding length and copper losses in Zone 1. This is advantageous since Fig. 6 shows that volume is minimized with low aspect ratio.

Single-layer winding efficiency is lower than for a toroidal winding over all the aspect ratios because the coil pitch must be sized for a two-pole layout to achieve variable-pole operation. Double-layer windings (3) and (4) are more efficient than toroidal windings in high aspect ratio Zone 2. Flux cancellation of double-layer windings leads to lower efficiency at either high or low speeds. Although option (4) is most efficient in Zone 2 at ω_b, it is the least efficient option at $\omega_{\max}$ because of the poor winding factor in the two-pole operation.

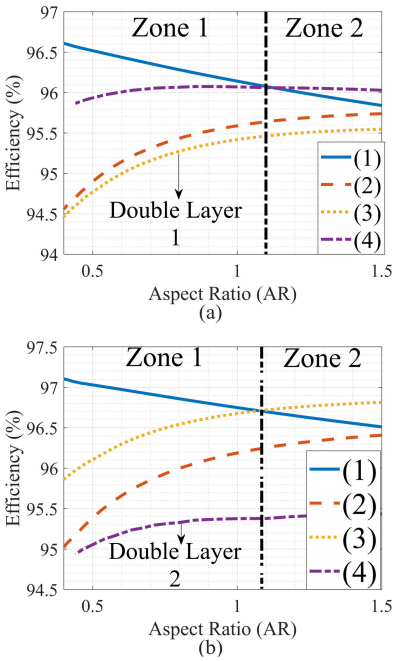

Fig. 7. Aspect ratio impact on electrical efficiency for the four winding types: (1) toroidal, (2) single-layer, (3) double-layer designed at $p_{\min}$, and (4) double-layer designed at $p_{\max}$ at (a) base and (b) maximum speeds. Toroidal windings are the most efficient in the low aspect ratio Zone 1.

C. Design Summary

Table V shows comparison of the toroidal, single-, and double-layer windings for a variable-pole IM designed to meet the specifications in Table III and refined using FEA. Toroidal machine (a) with aspect ratio 0.4 has the smallest volume and highest efficiency. Distributed winding designs (b)–(d) are selected to have an aspect ratio of 0.8 to maintain high efficiency without significantly increasing the volume.

TABLE VI
MACHINE EQUIVALENT CIRCUIT PARAMETERS FOR THE DESIGNS OF TABLE V, BASED ON FEA

	(a)	(b)	(c)	(d)
R_s (Ω)	0.11	0.09	0.072	0.11
R_r (Ω)	0.068	0.037	0.0313	0.06
L_{ls} (mH)	0.96	0.86	0.63	1.1
L_{lr} (mH)	1.14	0.55	0.61	1.6
$L_{m,6}$ (mH)	17.4	7.4	6.1	N/A
$L_{m,4}$ (mH)	39.2	N/A	N/A	19.2
$L_{m,2}$ (mH)	157	66	69	50.2

Option (d) is most efficient among distributed winding layouts because, unlike (b) and (c), its coil is sized for the four-pole operation. Design (d) has low core losses because it delivers peak torque using a four-pole configuration rather than a six-pole configuration. However, design (d) has the largest volume because it must deliver rated torque in the four-pole operation and requires a larger back yoke.

The toroidal design has the lowest copper loss because the low aspect design, combined with a small back yoke, minimizes the stator coil length. This also explains why the toroidal configuration has low leakage even though it has an extra return path outside the core that does not contribute to torque production. The toroidal design with low aspect ratio has the highest rated efficiency, smallest volume and weight, and has the highest torque capability at $\omega_{\max}$.

IV. COMPARISON OF WINDING DESIGNS OVER THE ENTIRE TORQUE–SPEED REGIME

Traction applications operate over wide torque–speed ranges and rarely operate at rated conditions. This section shows comparison of an 18-leg variable-pole design with three-leg fixed-pole designs. The torque–speed envelops of the winding configurations are compared. The efficiency maps over the entire torque–speed regime are presented and discussed.

A. Torque–Speed Envelope

To plot the torque–speed envelope generated by these winding configurations, a detailed variable-pole IM model that captures the impact of pole count p on machine parameters is needed. The parameters are obtained using FEA and RMxprt and are shown in Table VI. These parameters can be estimated using models in [26] and [12]. The impact of pole count on machine parameters is captured mainly in the magnetizing inductance $L_{m,p}$ [11], [12], [31]

$$L_m,\, p = \frac{C_p Q_s \mu_0 D l_e {N_c}^2 {k_{w,p}}^2 k_{\text{sat}}}{\pi g_e p^2 C_p} \tag{18}$$

where N_c is the turns count per slot, C_s and C_p are the number of series and parallel connected windings, respectively, g_e is the effective airgap length including the Carter coefficient [9], and k_{sat} is a saturation factor. Turns count N_c is selected based on ω_b

$$N_c = \frac{2 M_{\max} V_{\text{dc}}}{k_w B_g D l_e \omega_b C_s} \tag{19}$$

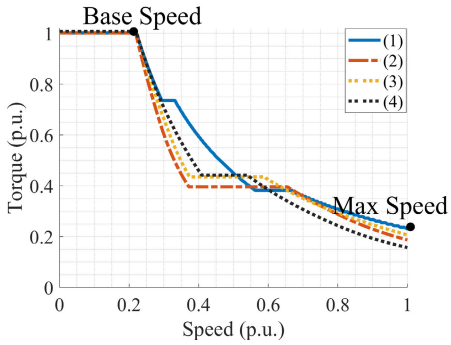

Fig. 8. Torque–speed envelope of variable-pole IMs for the winding configurations of Fig. 2. ω_b and $\omega_{\max}$ are the base and maximum speed, respectively. All the machines are designed to meet the torque requirement of Table III at ω_b. Pole count is selected to maximize the torque–speed envelop while operating within the current, voltage, and flux ratings.

where V_{dc} is the dc link voltage, and $M_{\max}$ is the maximum drive modulation index.

Fig. 8 shows the torque–speed envelope for these configurations. All the designs deliver rated torque through ω_b. Above ω_b, the toroidal winding maintains the largest envelope over most of the speed range and at $\omega_{\max}$, as it can reconfigure to the four-pole operation in the intermediate speed range and has lower leakage. In a narrow speed range around 0.6 p.u., double-layer option (c) has higher torque capability than the toroidal option because it is overdesigned due to the poor winding factor at six poles and reconfigured in that region to two poles which has a high winding factor. Double layer (d) also has higher torque capability around 0.6 p.u. speeds compared with the toroidal option because it has a thicker back yoke, as it is designed to deliver peak torque at a four-pole rather than a six-pole configuration, which allows for a larger airgap flux density in the two-pole operation. However, this same reason constrains design (d) to the lowest torque at $\omega_{\max}$ because its two-pole configuration enters flux weakening at a lower speed than for other designs. Single-layer design (b) and its short-pitched double-layer version (c) have lower torque capability at $\omega_{\max}$ compared with the toroidal design because long end turns produce extra leakage.

B. Efficiency Comparison Over Entire Torque–Speed Range

This section shows comparison of the electrical efficiencies over the entire torque–speed regime. Core losses are obtained using a transient FEA simulation. Copper losses are obtained based on the stator and rotor resistances obtained using RMxprt. End-winding leakage and copper losses for distributed winding designs are also determined using RMxprt. For toroidal windings, the leakage and resistance of the extra conductor on top of the winding are assumed to be equal to those of the slot conductor. The winding temperature is set to 50 °C. The loss minimization approach proposed in [11], is used to select the pole count at each operating point, as shown in Figs. 9 and 10 illustrates this method by showing the copper and core loss distribution for the toroidal configuration. The highest pole count $p_{\max}$ is only used near peak torque where the peak core and copper losses occur. Transitioning to lower pole counts at partial loads improves the efficiency

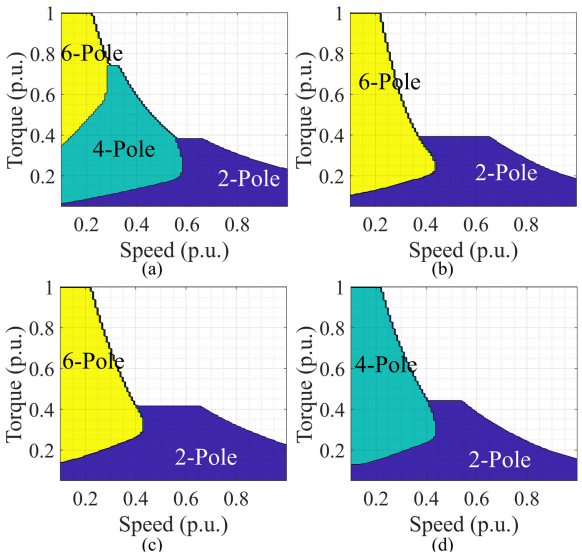

Fig. 9. Pole count selection for motor options in Table V. (a) Toroidal design 1, (b) single-layer design 2, (c) double-layer design 3, and (d) double-layer design 4.

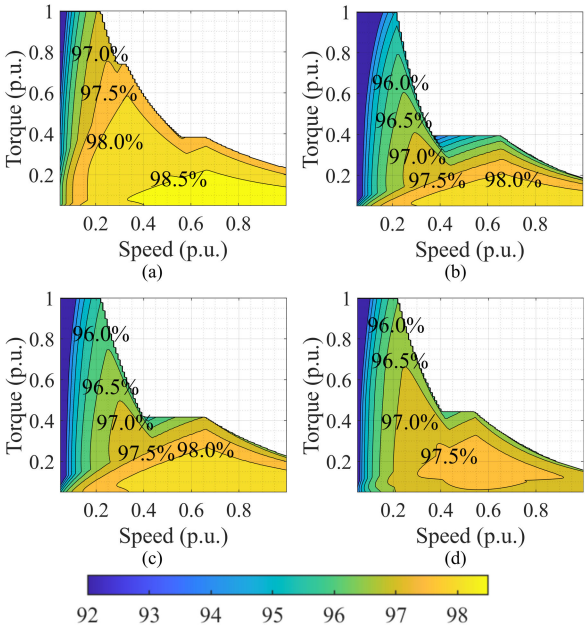

Fig. 10. Electrical efficiency colormap of designs summarized in Table V. Copper and core losses are obtained using FEA at 50 °C. (a) Toroidal design 1, (b) single-layer design 2, (c) double-layer design 3, and (d) double-layer design 4.

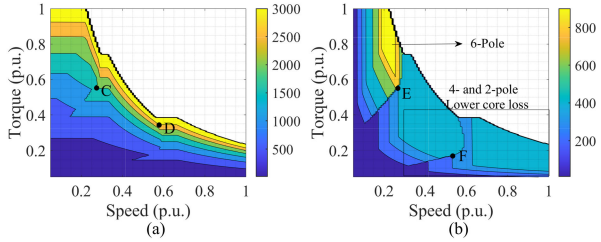

Fig. 11. (a) Copper and (b) core loss distribution for the toroidal winding layout. Operating points C and E are example of the six- to four-pole transition points while D and F are the four- to two-pole transitions. Switching to lower pole enlarges lower loss contour maps and particularly results in low core losses at high speeds.

by enlarging lower loss contours. The four-pole configuration improves the efficiency at intermediate torque and speeds

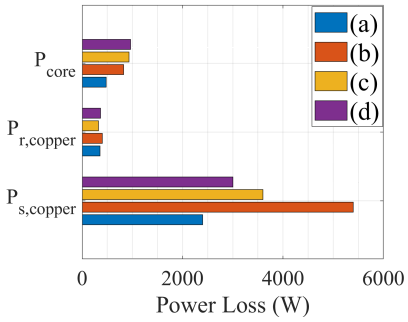

Fig. 12. Loss breakdown at rated torque and base speed. (a) Toroidal design and (b) and (c) distributed single- and double-layer designs are using a six-pole configuration while (d) is configured for the four-pole operation.

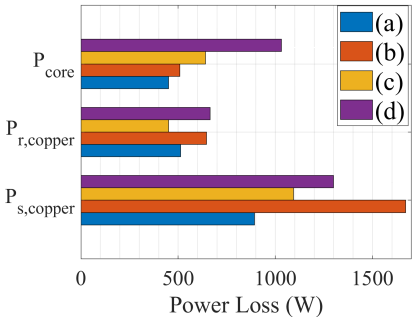

Fig. 13. Loss breakdown at a speed and torque of 0.8 and 0.2 p.u., respectively. This represents high-speed low-torque operation, and all the motors are using a two-pole configuration. (a) Toroidal design 1, (b) single-layer design 2, (c) double-layer design 3, and (d) double-layer design 4.

while the two-pole configuration is the most efficient for low torque levels and high speeds due to lower core losses [11]. Fig. 10 shows efficiency colormaps of these designs. All are efficient at high speeds because they reconfigure to the two-pole operation, which reduces ac and core losses by shifting to a lower fundamental frequency. The extra flexibility of toroidal design (a) improves the efficiency in the intermediate torque–speed range. Single-layer design (b) has the lowest efficiency near rated torque because its windings are long which leads to high copper loss, as shown in Fig. 12. The short-pitched version of this winding, as in option (c), improves the efficiency map by reducing the winding length and stator copper loss, especially near rated torque. Double-layer design approach (d) has higher efficiency near rated torque than other distributed winding options because of lower stator copper loss due to shorter windings. However, option (d) has lower efficiency at high speed compared with other designs, as seen in Fig. 9. Fig. 13 shows that the lower efficiency of option (d) is linked to higher core loss. This is a direct consequence of designing the machine to deliver peak torque in its four-pole configuration, which requires a thicker yoke. This leads to larger core volume and flux density in the two-pole operation compared with the other designs. The poorer winding factor of option (d) in the two-pole operation also contributes to additional core and copper losses.

To summarize, a single-layer design is the least efficient option near rated torque for a variable-pole IM due to high stator copper losses. For low-speed and high-torque operation, toroidal design (a) has the highest efficiency. This is because the toroidal winding uses a low aspect ratio, leading to lowest

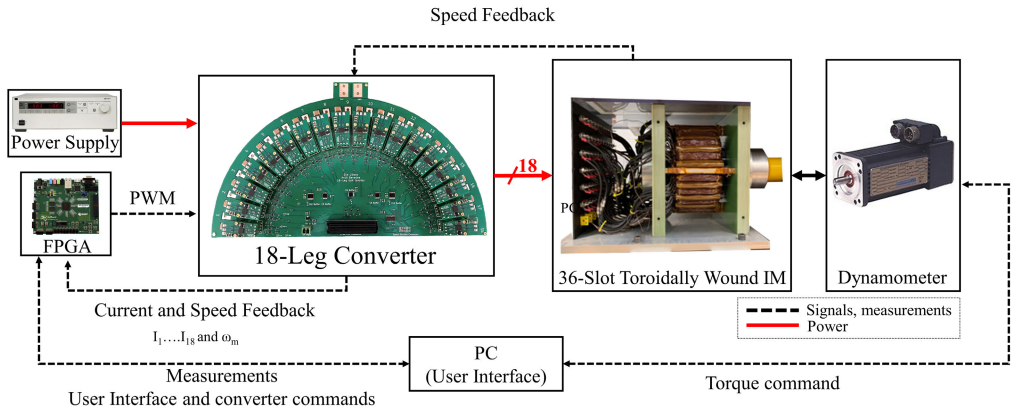

Fig. 14. Experimental setup and test rig. An 18-leg converter is used to drive the variable-pole toroidally wound IM. This 18-leg converter includes individual phase current sensors, speed encoder, and analog-to-digital converters which are interfaced with an FPGA. The FPGA controls the converter PWM switching and logs the measurements in real-time to MATLAB Simulink to record losses and speed. The dynamometer is used to command load torque through LabVIEW.

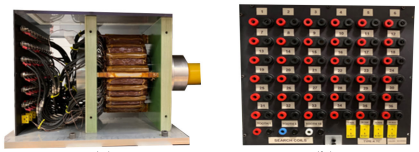

Fig. 15. (a) Side and (b) front views of the experimental toroidally wound 36-slot IM.

TABLE VII
EXPERIMENTAL MOTOR SPECIFICATIONS

Quantity	Value
dc bus voltage V_{dc} (V)	70
Phase current I_{phase} (A)	4.5
Peak torque (N·m)	3.4
Base speed (RPM)	900
Maximum speed (RPM)	3300
Fundamental frequency at maximum speed (Hz)	55
Power factor	0.7
Stator slots Q_s	36
Inner diameter D (mm)	100
Stack length l_e (mm)	71
Aspect ratio	0.71
Effective slot area A_{slot} (cm^2)	19
Rotor surface area A_{core} (cm^2)	223
Current density J_s (A/mm^2)	3.4

stator copper loss, as shown in Fig. 12. The toroidal design has less core loss because of its smaller core volume and better winding factor. Overall, a toroidal design is highly efficient over the entire torque–speed regime. Double-layer designs are an efficient alternative to toroidal windings, but are constrained in certain operating regimes. All the designs have high efficiency over a wide operating regime because of variable-pole operation and a copper rotor.

V. EXPERIMENTAL SETUP AND RESULTS

Fig. 14 shows the experimental setup. A toroidally wound 36-slot IM with external access to all its slots, shown in Fig. 15, is driven by an 18-leg converter. Table VII provides the specifications of the experimental machine and drive system. The detailed design and pole-changing operation of the 18-leg drive is provided in [8]. The dynamometer is controlled through LabVIEW to load the motor. A Zedboard FPGA is used to command inverter pulsewidth modulation and record current and speed measurements. The current and voltage values are logged to MATLAB Simulink in real-time to compute the motor electrical input power. The output power is computed by multiplying the commanded torque in LabVIEW by the motor speed. These measurements are used to calculate the experimental losses in the motor which include electrical copper and core losses and mechanical losses due to the nonideal coupling of the motor and dynamometer. The inverter achieves electronic pole changing by modulating phase shift as in Table I, and Fig. 16 shows the stator currents in the 18 toroidal coils at two, four, and six poles. Switching harmonics are low in the currents which have a pure sinsoidal shape because reconfiguring to lower poles lowers the fundamental frequency (55 Hz) and using a high number of inverter legs enables high switching frequency (50 kHz) [8]. This unique advantage of variable-pole designs could be used to minimize additional motor losses and torque ripple caused by PWM switching.

Each pair of adjacent slots (slots 1 and 2, 3, and 4 etc.) are connected in series to form the 18-terminal winding configuration shown in Fig. 17. The winding can be reconfigured to emulate a single-layer winding by externally connecting slots which are 180° apart (e.g., slots 1 and 19), as shown in Fig. 18, although the leakage inductance and resistance will differ from a conventional single-layer winding. This approach can be used to investigate benefits gained from a toroidal winding's extra flexibility. Fig. 19 shows the torque–speed characteristics for the six-, four-, and two-pole operations. Beyond points 1 and 2, the four- and two-pole configurations have higher torque capability than six-pole, respectively. Because a toroidal winding has the flexibility to reconfigure to the four-pole operation, it has higher torque capability in the

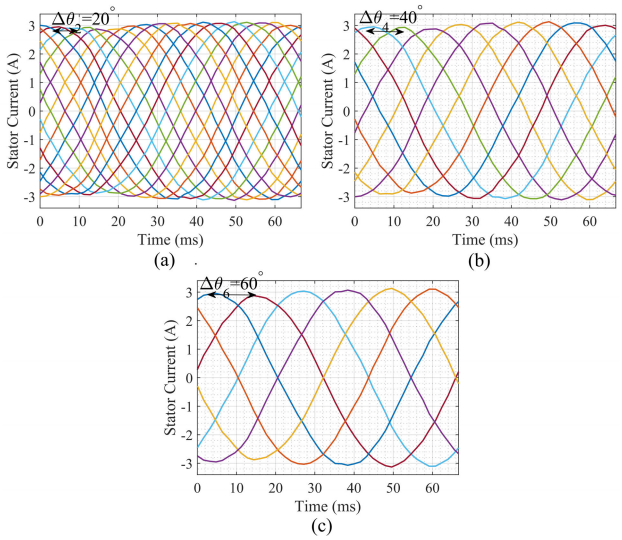

Fig. 16. Experimental 18-leg drive currents with toroidal winding at (a) two-, (b) four-, and (c) six-pole operations matching the excitation pattern of Table I.

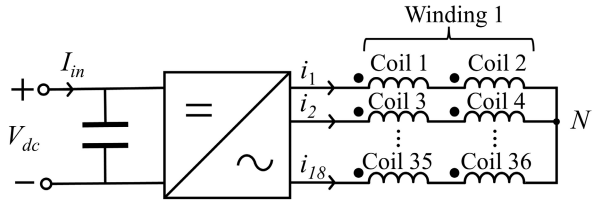

Fig. 17. Winding and drive configuration for toroidally wound IM with 36 slots. Each pair of adjacent torodial coils, physically spaced by 10°, is grouped in series to form a winding.

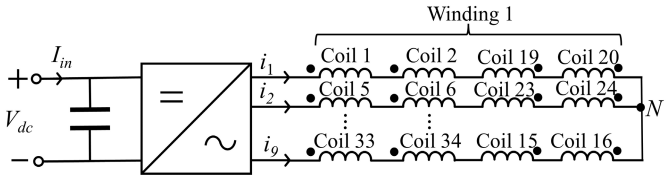

Fig. 18. Winding and drive configuration to emulate a single-layer winding. Coils which are 180° apart are connected in series to form a two-pole/nine-phase winding.

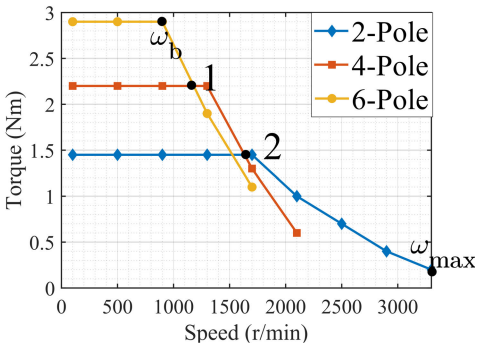

Fig. 19. Experimental torque versus speed characteristics for the six-, four-, and two-pole configurations. Variable-pole operation improves the high-speed torque capability by shifting to the four- and two-pole operations at points 1 and 2, respectively [8].

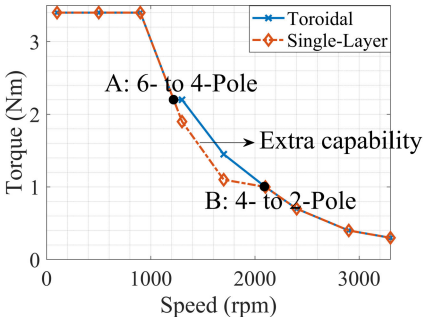

Fig. 20. Experimental torque versus speed characteristic for toroidal and emulated single-layer winding. Toroidal windings have extra capability in the intermediate speed range due to the four-pole operation.

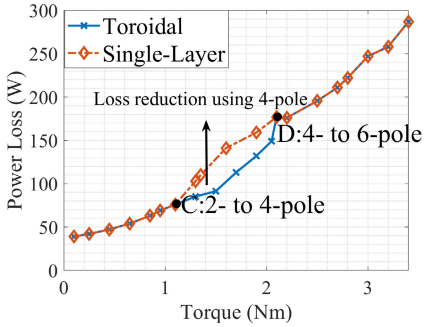

Fig. 21. Experimental power loss versus torque for toroidal and emulated single-layer windings at 900 rpm. Toroidal windings have lower loss in the intermediate torque range due to the four-pole operation.

intermediate speed range (between points A and B), as shown in Fig. 20. Both the configurations can improve high-speed torque beyond point B by shifting to the two-pole operation. The torque available with a toroidal winding is higher than for an ideal single-layer winding at maximum speed because of lower leakage. Here, the experimental torques are the same for both the arrangements since the single-layer winding is emulated using the same toroidal winding. Figs. 21 and 22 show comparison of experimental loss versus torque at 900 and 1300 rpm, respectively. Reconfiguration to the four-pole operation reduces losses at intermediate torque levels at 900 rpm between points C and D. At 1300 rpm, a four-pole configuration reduces loss significantly for any torque above 1 N · m. Thus, the extra flexibility of toroidal windings to reconfigure to four-pole reduces losses intermediate torque and speed range compared with conventional single-layer design.

Fig. 23 shows the experimental motor current and speed when two phases are out, which leads to voltage imbalances. The motor maintains its average 900 rpm speed at the cost of an increase in phase current amplitude and current imbalances. Thus, the high number of inverter legs used with the toroidal design improves the fault tolerance. In addition, this 18-leg converter has lower thermal stress and higher efficiency compared with a three-leg converter with the same rating [8].

While the IM was rewound (the original motor is WEG model # 00536OT3E182T) and not designed to have the best possible aspect ratio for a toroidal winding, it is used to validate the analytical models used in Section III. Analytical torque, calculated using (10), matches with the experimental result within 10%, as shown in Table VIII. Moreover, the detailed loss model of Section III-B, which estimates copper and core losses for all winding designs, is within 12% of the

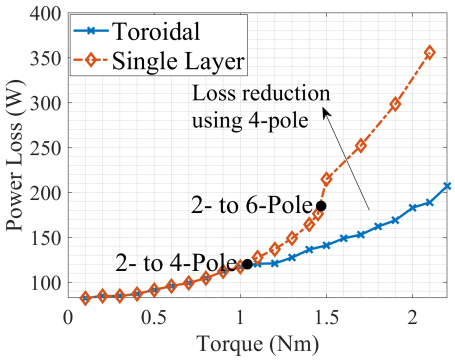

Fig. 22. Experimental power loss versus torque for toroidal and emulated single-layer windings at 1300 rpm. Toroidal windings have lower loss near peak torque because a four-pole configuration is used rather than a six-pole configuration.

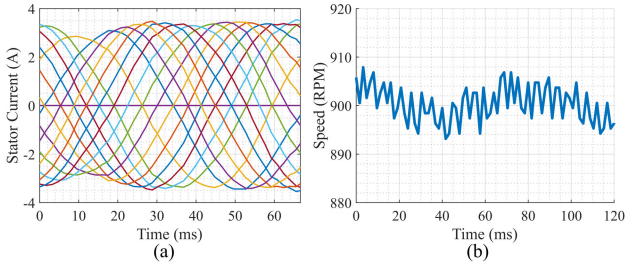

Fig. 23. Experimental (a) currents and (b) speed when two phases are out (open-circuit) under the following conditions: $f = 15$ Hz and $T_e = 0.9$ N·m. The motor speed is maintained at 900 rpm even with two phases out at the cost of higher current per phase compared with Fig. 16 and phase imbalances.

TABLE VIII
FRAMEWORK VALIDATION USING EXPERIMENTAL MOTOR

Quantity	Theoretical	Experimental
Rated torque T_e (Nm)	3.7	3.4
Rated power loss (W)	305	270
L_{m6} (mH)	10.3	9.4
L_{m4} (mH)	22.6	25.7
L_{m2} (mH)	86.8	80.6

measured value. The dependence of the magnetizing inductance on pole count is verified through no-load testing. These key results, summarized in Table VIII, validate the proposed design framework used to assess the impact of aspect ratio on efficiency and volume and compare the four variable-pole winding design alternatives.

VI. CONCLUSION

This article investigated four winding design approaches for a variable-pole IM based on toroidal and distributed single- and double-layer windings. An analytical framework, combined with FEA simulations, was used to compare the efficiency, power density, and torque–speed envelop of these windings. A toroidal design is most flexible for pole changing but it is critical to design it with a low aspect ratio to maximize efficiency and power density. A single-layer distributed winding suffers from long coil pitch in a variable-pole application because it is designed at the lowest pole count. This leads to high leakage and losses. Double-layer designs are an efficient solution but can only match the efficiency of a low aspect ratio toroidal design at either low or high speed but not both. An experimental 36-slot toroidally wound IM driven by an 18-leg converter was used to validate the design framework. The toroidal setup was also configured externally to emulate a single-layer winding. Efficiency and torque–speed envelop improvements are achieved with a toroidal configuration compared with single-layer windings because of extra pole-changing flexibility. The 18-leg toroidal design also showed fault tolerance capability by maintaining its speed under voltage imbalances caused by having two faulty phases at the cost of higher current amplitude and imbalance. This article shows that a toroidally wound IM designed with a low aspect ratio has high power density, efficiency, and fault tolerance over the wide operating torque–speed regime needed in an EV application.

REFERENCES

[1] J.-R. Riba, C. López-Torres, L. Romeral, and A. Garcia, "Rare-Earth-free propulsion motors for electric vehicles: A technology review," *Renew. Sustain. Energy Rev.*, vol. 57, pp. 367–379, May 2016.

[2] A. M. Bazzi, Y. Liu, and D. S. Fay, "Electric machines and energy storage: Over a century of technologies in electric and hybrid electric vehicles," *IEEE Electrific. Mag.*, vol. 6, no. 3, pp. 49–53, Sep. 2018.

[3] A. Harson, "Design considerations for induction machines for electric vehicle drives," in *Proc. 7th Int. Conf. Electr. Mach. Drives*, 1995, pp. 16–20.

[4] N. Zhao and N. Schofield, "An induction machine design with parameter optimization for a 120-kW electric vehicle," *IEEE Trans. Transport. Electrific.*, vol. 6, no. 2, pp. 592–601, Jun. 2020.

[5] G. Pellegrino, A. Vagati, B. Boazzo, and P. Guglielmi, "Comparison of induction and PM synchronous motor drives for EV application including design examples," *IEEE Trans. Ind. Appl.*, vol. 48, no. 6, pp. 2322–2332, Nov./Dec. 2012.

[6] Z. Yang, F. Shang, I. P. Brown, and M. Krishnamurthy, "Comparative study of interior permanent magnet, induction, and switched reluctance motor drives for EV and HEV applications," *IEEE Trans. Transport. Electrific.*, vol. 1, no. 3, pp. 245–254, Aug. 2015.

[7] E. Libbos, R. Hao, B. Ku, A. Banerjee, and P. T. Krein, "Modular multiphase drives for variable-pole induction machines in electric vehicles," in *Proc. IEEE Appl. Power Electron. Conf. Expo. (APEC)*, Mar. 2020, pp. 696–703.

[8] E. Libbos, E. Krause, A. Banerjee, and P. T. Krein, "Inverter design considerations for variable-pole induction machines in electric vehicles," *IEEE Trans. Power Electron.*, vol. 37, no. 11, pp. 13554–13565, Nov. 2022.

[9] M. Osama and T. A. Lipo, "A new inverter control scheme for induction motor drives requiring wide speed range," *IEEE Trans. Ind. Appl.*, vol. 32, no. 4, pp. 938–944, Jul. 1996.

[10] J. M. Miller, V. Stefanovic, V. Ostovic, and J. Kelly, "Design considerations for an automotive integrated starter-generator with pole-phase modulation," in *Proc. Conf. Rec. IEEE Ind. Appl. Conf. 36th IAS Annu. Meeting*, Sep. 2001, pp. 2366–2373.

[11] E. Libbos, B. Ku, S. Agrawal, S. Tungare, A. Banerjee, and P. T. Krein, "Loss minimization and maximum torque-per-ampere operation for variable-pole induction machines," *IEEE Trans. Transport. Electrific.*, vol. 6, no. 3, pp. 1051–1064, Sep. 2020.

[12] M. Magill, "An investigation of electronic pole changing in high inverter count induction machines," Univ. Illinois Urbana-Champaign, Champaign, IL, USA, Tech. Rep., UILU-ENG2015-2505, CEME-TR-2015-01, Apr. 2015.

[13] E. Libbos, B. Ku, S. Agrawal, S. Tungare, A. Banerjee, and P. T. Krein, "Variable-pole induction machine drive for electric vehicles," in *Proc. IEEE Int. Electric Mach. Drives Conf. (IEMDC)*, May 2019, pp. 515–522.

[14] B. P. Reddy, B. S. Umesh, A. M. Rao, B. V. R. Kumar, and K. S. Kumar, "A five speed 45-phase induction motor drive with pole phase modulation for electric vehicles," in *Proc. IEEE Int. Conf. Ind. Technol. (ICIT)*, Mar. 2017, pp. 258–263.

[15] M. Osama and T. A. Lipo, "Modeling and analysis of a wide-speed-range induction motor drive based on electronic pole changing," *IEEE Trans. Ind. Appl.*, vol. 33, no. 5, pp. 1177–1184, Sep. 1997.
[16] S. Mallampalli, Z. Q. Zhu, J. C. Mipo, and S. Personnaz, "Six-phase pole-changing winding induction machines with improved performance," *IEEE Trans. Energy Convers.*, vol. 36, no. 1, pp. 534–546, Mar. 2021.
[17] B. S. Umesh and K. Sivakumar, "Pole-phase modulated multiphase induction motor drive with reduced torque ripple and improved DC link utilization," *IEEE Trans. Power Electron.*, vol. 32, no. 10, pp. 7862–7869, Oct. 2017.
[18] B. P. Reddy, M. Meraj, A. Iqbal, S. Keerthipati, and M. S. Bhaskar, "A hybrid multilevel inverter scheme for nine-phase PPMIM drive by using three-phase five-leg inverters," *IEEE Trans. Ind. Electron.*, vol. 68, no. 3, pp. 1895–1904, Mar. 2021.
[19] J.-Q. Yang, R.-S. Yin, X.-J. Zhang, and J. Huang, "Exponential response electrical pole-changing method for a five-phase induction machine with a current sliding mode control strategy," *Frontiers Inf. Technol. Electron. Eng.*, vol. 18, no. 8, pp. 1151–1166, Aug. 2017.
[20] B. S. Umesh, N. K. Kumar, and K. Sivakumar, "Performance improvement of a nine phase pole phase modulated induction motor drive," in *Proc. IEEE Int. Conf. Ind. Technol. (ICIT)*, Mar. 2015, pp. 812–817.
[21] A. Iqbal, B. P. Reddy, S. Rahman, and M. Meraj, "Modelling and indirect field-oriented control for pole phase modulation induction motor drives," *IET Power Electron.*, vol. 16, no. 2, pp. 268–280, Feb. 2023.
[22] B. Ge, D. Sun, W. Wu, and F. Z. Peng, "Winding design, modeling, and control for pole-phase modulation induction motors," *IEEE Trans. Magn.*, vol. 49, no. 2, pp. 898–911, Feb. 2013.
[23] P. L. Alger, *The Nature of Polyphase Induction Machines*. Hoboken, NJ, USA: Wiley, 1951.
[24] M. Van Der Giet, K. Hameyer, and S. Risse, "Induction motor with pole-changing winding for variable supply frequency," in *Proc. IEEE Int. Electric Mach. Drives Conf.*, May 2007, pp. 1484–1489.
[25] E. F. Fuchs, J. Schraud, and F. S. Fuchs, "Analysis of critical-speed increase of induction machines via winding reconfiguration with solid-state switches," *IEEE Trans. Energy Convers.*, vol. 23, no. 3, pp. 774–780, Sep. 2008.
[26] T. A. Lipo, *Introduction to AC Machine Design*. Hoboken, NJ, USA: Wiley, 2017.
[27] N. Riviere, M. Villani, and M. Popescu, "Optimisation of a high speed copper rotor induction motor for a traction application," in *Proc. 45th Annu. Conf. IEEE Ind. Electron. Soc.*, Oct. 2019, pp. 2720–2725.
[28] M. Popescu, N. Riviere, G. Volpe, M. Villani, G. Fabri, and L. Di Leonardo, "A copper rotor induction motor solution for electrical vehicles traction system," in *Proc. IEEE Energy Convers. Congr. Expo. (ECCE)*, Sep. 2019, pp. 3924–3930.
[29] S. Huang, J. Luo, F. Leonardi, and T. A. Lipo, "A general approach to sizing and power density equations for comparison of electrical machines," *IEEE Trans. Ind. Appl.*, vol. 34, no. 1, pp. 92–97, Jan./Feb. 1998.
[30] Y. Wan, Q. Li, J. Guo, and S. Cui, "Thermal analysis of a Gramme-ring-winding high-speed permanent-magnet motor for pulsed alternator using CFD," *IET Electr. Power Appl.*, vol. 14, no. 11, pp. 2202–2211, Nov. 2020.
[31] M. P. Magill, P. T. Krein, and K. S. Haran, "Equivalent circuit model for pole-phase modulation induction machines," in *Proc. IEEE Int. Electr. Mach. Drives Conf. (IEMDC)*, May 2015, pp. 293–299.

Elie Libbos (Graduate Student Member, IEEE) received the B.E. degree (Hons.) in electrical and computer engineering (ECE) from the American University of Beirut (AUB), Beirut, Lebanon, in 2018, and the M.S. degree in electrical engineering from the University of Illinois at Urbana-Champaign (UIUC), Urbana, IL, USA, in 2020, where he is currently pursuing the Ph.D. degree.

He has interned with Kilby Labs, Texas Instrument, Dallas, TX, USA, in 2022. His research interests include power electronics and electric machines and drives for electric vehicles.

Mr. Libbos has received the ECE Distinguished Graduate Award from AUB in 2018. As a Graduate Student, he has been awarded the ECE Distinguished Research Fellowship, UIUC.

Elisa Krause (Graduate Student Member, IEEE) received the B.S. degree in electrical engineering from the University of Illinois at Urbana-Champaign (UIUC), Urbana, IL, USA, in 2022. She is currently pursuing the Bachelor of Science degree in electrical engineering with the University of California at Berkeley, Berkeley, CA, USA.

Her research interests include power electronics, specifically in hybrid switched-capacitor circuits.

Arijit Banerjee (Senior Member, IEEE) received the B.E. degree in electrical engineering from Bengal Engineering and Science University, Howrah, India, in 2005, the M.Tech. degree in electrical engineering from IIT Kharagpur, Kharagpur, India, in 2007, and the Ph.D. degree in electrical engineering from the Massachusetts Institute of Technology, Cambridge, MA, USA, in 2016.

He was with the Power Conversion Systems Group, General Electric Global Research Centre, Bengaluru, India, where he has worked on monitoring and diagnostics of electromechanical systems using electrical signatures. From 2006 to 2007, he was a Visiting Student with the Institute for Power Electronics and Control of Drives, Technische Universität Darmstadt, Darmstadt, Germany, through the German Academic Exchange Service Fellowship. He is currently an Assistant Professor with the Department of Electrical and Computer Engineering, University of Illinois at Urbana-Champaign, Urbana, IL, USA. He holds 18 issued patents. His research interests include analysis, design, control, and diagnostics of electromechanical energy conversion systems.

Dr. Banerjee is a Senior Member of the U.S. National Academy of Inventors and an Associate Editor of IEEE TRANSACTIONS ON INDUSTRY APPLICATIONS.

Philip T. Krein (Life Fellow, IEEE) received the B.S. degree in electrical engineering and the B.A. degree in economics and business from the Lafayette College, Easton, PA, USA, in 1978, and the M.S. and Ph.D. degrees in electrical engineering from the University of Illinois at Urbana-Champaign, Urbana, IL, USA, in 1980 and 1982, respectively.

He was an Engineer with Tektronix, Beaverton, OR, USA, and then returned to the University of Illinois at Urbana-Champaign. He was a Senior Fulbright Scholar with the University of Surrey, Guildford, U.K., from 1997 to 1998. From 2003 to 2014, he was the Founder and the Director of SolarBridge Technologies, Inc., Austin, TX, USA, as the company developed ac photovoltaic panels. From 2016 to 2020, he was the Executive Dean of the Zhejiang University/University of Illinois at Urbana-Champaign Institute, Haining, China. He holds the Grainger Endowed Chair Emeritus in electric machinery and electromechanics at the University of Illinois at Urbana-Champaign and is an Adjunct Distinguished Professor with Zhejiang University, Hangzhou, China. He holds 42 U.S. patents. His current research interests include all aspects of power electronics, machines, drives, and electric transportation, with an emphasis on nonlinear control approaches.

Dr. Krein is a fellow of the U.S. National Academy of Inventors and a member of the U.S. National Academy of Engineering. He has received the IEEE William E. Newell Power Electronics Award in 2003 and the IEEE Transportation Technologies Award in 2021. He was the President of the IEEE Power Electronics Society, a member of the IEEE Board of Directors, and the Chair of the IEEE Transportation Electrification Community. He is a Registered Professional Engineer in Illinois and Oregon. He is an Associate Editor of the IEEE OPEN JOURNAL OF POWER ELECTRONICS.